Catalysis Science & Technology

ROYAL SOCIETY OF CHEMISTRY

PAPER

View Article Online
View Journal | View Issue



Cite this: *Catal. Sci. Technol.*, 2025, 15, 6703

# Modeling the shape and stability of supported Co nanoparticles under Fischer–Tropsch conditions *via* DFT calculations and Monte Carlo simulations: insights into CO-driven surface reconstruction

Enrico Sireci, [a] Tilman D. Grüger,[a] Philipp N. Plessow, [a] Dmitry I. Sharapa [a] and Felix Studt *[ab]

In this work, we have expanded our recently published combined density functional theory (DFT) – Monte Carlo (MC) approach to model supported Co nanoparticles (NPs) to include the effects of Co–CO interactions. We derived coordination number (CN) – specific energy corrections based on DFT-calculated $\Delta G_{ads}$ of CO on different Co facets and incorporated them in our energy model. This allowed us to simulate supported Co NPs with increasing size under Fischer–Tropsch (FT) operating conditions, both at high and low CO conversion ($X_{CO}$). Our results reveal drastic surface reconstruction induced by CO, that consists of a contraction of the close-packed surfaces in favor of B5-A step sites. This transformation drives the NPs from a highly faceted toward a rounder shape, and is accompanied by the appearance of triangular terraces previously reported experimentally. The increase of the concentration of B5-A sites, on which CO can dissociate, is speculated to enhance catalyst activity. Additionally, we demonstrate that CO significantly lowers the surface energy of Co NPs, profoundly influencing their redox behavior and stability. While CO reduces the thermodynamic driving force for sintering, its positive impact on sintering kinetics is likely dominant. Our study provides a comprehensive theoretical description of fcc Co NPs under operating conditions, accounting simultaneously for the effects of particle size, temperature and both metal–support and metal–adsorbate interactions.

Received 28th July 2025,
Accepted 26th September 2025

DOI: 10.1039/d5cy00921a

rsc.li/catalysis



## Introduction

Supported Co catalysts are the gold standard for sustainable aviation fuels (SAFs) production *via* the Fischer–Tropsch synthesis. The widely reported[1–12] size-dependent turnover frequency (TOF) of Co nanoparticles (NPs) has prompted previous theoretical studies[13–18] to investigate their structures as a function of particle size. Despite the significant insights provided by these previous works, their simulations only included NPs in vacuum and thus neglected the effect of the gas-phase under operating conditions. However, CO is known to strongly bind to Co and previous experimental and theoretical studies have suggested that it might induce significant surface reconstruction.[1,19–23] Thus, these models are representative of catalysts operating at low pressures, conditions that might be relevant for specific research applications but are rather far from the way the industrial process is carried out. Other studies[24–26] have modelled Co NPs in a CO gas phase employing the classical Wulff construction, that, despite offering significant perspectives, inherently fails to capture complex effects such as particle size and the presence of surface defects.

In our recent work,[18] we have introduced a new method involving DFT and Monte Carlo (MC) simulations to model Co NPs structures and energetics including the effects of particle size ($D_{Co}$), temperature and metal–support interactions (MSI). This was done by deriving a model from DFT calculations describing the energy of Co atoms with changing coordination number (CN)[27–29] as well as the Co-support adhesion energies ($\gamma_{adh}$), and by employing it in a MC algorithm that redistributes Co atoms in a fcc grid. Our results showed that the concentration of step and kink sites increases with $D_{Co}$, and that while increasing MSI led to lower dispersion and to flattening of the NPs, they hardly affected the site distribution. Additionally, we were able to obtain surface energies ($\gamma$) and chemical potentials ($\Delta\mu_{Co}$) of realistic fcc Co NPs without resorting to several approximations previous studies had to rely on.

[a] *Institute of Catalysis Research and Technology, Karlsruhe Institute of Technology, Hermann-von-Helmholtz-Platz 1, 76344 Eggenstein-Leopoldshafen, Germany. E-mail: felix.studt@kit.edu*
[b] *Institute for Chemical Technology and Polymer Chemistry, Karlsruhe Institute of Technology, Engesserstrassse 18, 76131 Karlsruhe, Germany*

In this work, we expand our methodology to account also for the effects of Co–CO interactions. These were straightforwardly included in our approach by calculating Gibbs free energies of adsorption of CO ($\Delta G_{ads}$) at 500 K on different Co facets, from which we derived CN-specific energy corrections. We show that CO-induced surface reconstruction has dramatic effects on the surface morphology as well as on the energetics of fcc Co NPs, and we discuss how these can be invoked to explain observations reported in numerous experimental studies. Importantly, our models now include a full *ab initio* description of Co NPs structures and stability accounting simultaneously for the effects of particles size, temperature, MSI and metal–adsorbate interactions. To the best of our knowledge, this work offers the most comprehensive theoretical modelling yet of fcc Co NPs under FT working conditions and hence improves the current understanding of supported Co catalysts.

# Computational methods

### DFT calculations

It is well-established that most of the widely used GGA functionals tend to overestimate CO adsorption energies[30] while underestimating metal surface energies, and new formulations that aimed at correcting one of these two issues made the other worse.[31] Accurate estimations of both quantities are crucial for this study, as the NPs structures and energies obtained from our models will largely depend on them. The BEEF-vdW[32] functional has been shown[30] to reconcile predictions of surface energies and adsorption energies of CO on Pt (111) and Rh (111) with reasonable errors as well as to predict accurate CO adsorption energies on Co (0001),[33] and was thus employed for the DFT calculations in this work. Additionally, in our previous study we have shown that the surface energy of fcc Co NPs (converged with $D_{Co}$) obtained from our models employing BEEF-vdW is very close to reported experimental values.[34] DFT calculations were performed within the software VASP version 6.2,[35,36] using the projector-augmented wave (PAW) method with standard PAW potentials.[37] Gaussian smearing with a width of 0.1 eV was used in all calculations and the sampling of the Brillouin zone was carried out in a Monkhorst–Pack grid with a *k*-point density of approximately 36 k-points $Å^{-1}$, that is a $(14 \times 14 \times 1)$ grid for the $(1 \times 1)$ fcc Co (111) surface. Bulk calculations were carried out with an energy cutoff of 600 eV, which was changed to 400 eV for all the other calculations. Convergence of the SCF cycle was set at an energy difference of $10^{-6}$ eV, while ionic convergence was achieved when atomic forces were below 0.01 eV $Å^{-1}$.

In our investigation on the effect of the gas phase on Co NPs, we mimicked industrial FT conditions considering $T$ = 500 K and a feed of 20 bar and $H_2$:CO = 2, both in high and low CO conversion ($X_{CO}$) scenarios. In the first, we considered $X_{CO}$ = 75%, resulting in $p_{CO}$ = 1.5 bar and $p_{H_2O}/p_{H_2}$ = 2.1, while in the second, $X_{CO}$ was set at 25%, resulting in $p_{CO}$ = 5 bar and $p_{H_2O}/p_{H_2}$ = 0.2. The $\Delta G_{ads}$ of CO at 500 K on the low index fcc Co facets were calculated at different coverages. The Co slabs were composed of 4 layers of which the bottom two were kept frozen in their bulk configuration. At least 15 Å of vacuum were used in all calculations. The reference gas-phase molecules, namely CO, $H_2$ and $H_2O$, were treated within the ideal gas framework, while adsorbed hydroxyl groups on the oxidic support slabs (considered for the $\gamma_{adh}$ calculations) and adsorbed CO on the Co surfaces were treated with the harmonic approximation. Vibrational analysis using the finite differences method with an atomic displacement of 0.02 Å were carried out to estimate zero-point-energies (ZPE), enthalpy changes from 0 to 500 K ($\Delta H^{0\rightarrow 500}$) and vibrational entropies ($S_{vib}$). The *xyz* coordinates and potential energies of the DFT-calculated structures are provided separately. For details about surface energies ($\gamma$) and $\gamma_{adh}$ calculations we direct the reader to our previous work.[18] Table S1 gives information about the structures used to calculated $\gamma_{adh}$ in the high and low $X_{CO}$ scenarios.

### Monte Carlo simulations

We direct the reader to our previous work for an extensive description of our MC simulations.[18] In short, we employ a lattice model in which Co atoms are redistributed in a fixed fcc grid. The energy of Co atoms ($E_{Co}$) is estimated based on their nearest-neighbor coordination number (CN). We employ a linear correlation between $E_{Co}$ and CN, obtained by estimating the energy difference between a bulk Co atom with CN = 12 and one with CN = 9 *via* the surface energy calculation of the (111) facet. The energy of a Co atom is reduced by $\gamma_{adh}$ when it is found next to the support, that is modelled as a slab of dummy atoms oriented along the (111) plane. We make use of the $\gamma_{adh}$ between fcc Co(111) and $SiO_2$(001), $CoAl_2O_4$(110), and $CoTiO_3$(0001) that are documented in our previous work,[18] and stress that these represent ideal oxide surfaces, and thus neglect the effect of surface roughness as well as the presence of defects or vacancies on the support. We acknowledge that these effects would likely alter the metal–support interactions but note that their investigation is beyond the scope of this work, that rather focuses on the effect of gas-phase CO on Co NPs morphologies and stabilities.

To include the effect of CO, a CN-specific energy correction based on the calculated $\Delta G_{ads}$ on different fcc Co facets is applied. The energy cost associated with removing CO adsorbed on the cobalt surface found at the metal–support interface is considered by applying a reduced adhesion energy equal to $\gamma_{adh} - \Delta G_{ads}(111)$ to Co atoms next to the support. 2 nm (376 atoms), 4 nm (3008 atoms), 6 nm (10 152 atoms), 8 nm (24 064 atoms) and 10 nm (47 000 atoms) NPs were simulated, with 40 independent runs carried out for each size. The reported quantities are averaged over the 40 lowest energy structures identified in each run; error bars correspond to the mean average deviations (MAD). We adopted the site identification scheme

 

proposed by van Hardeveld *et al.*,[38] that was already extensively employed to describe fcc and hcp Co NP surfaces,[13,16,17] and thus we considered 2B3, B4, B5-A, B5-B and B6 sites, corresponding to (111) terrace sites, (100) terrace site, (111)/(100) step sites, (111)/(111) step sites and kink sites, respectively. We note that albeit the van Hardeveld scheme is intrinsically not suitable to describe heavily reconstructed or amorphous sites, it is adequate to fully characterize the surface of our NP models as they are constrained into an ideal fcc lattice.

Convergence tests carried out in our previous work showed that $5 \times 10^{11}$ MC iterations were sufficient to ensure convergence of energies and site distributions for the largest (10 nm) particles.[18] We verified that this holds also here for the low $X_{CO}$ scenario (see Fig. S1) and have therefore used this number of iterations as threshold to stop the MC runs in the present work.

## Results and discussion

### $\Delta G_{ads}$ of CO on fcc Co

Within our lattice model, we make use of CN-specific energy corrections to account for the effect of CO on the NP shape. In order to do this, we used the outcome of DFT calculations simulating $\Delta G_{ads}$ of CO at 500 K on different fcc Co facets. The (111), (100) and (311) surfaces were chosen to calculate the corrections for Co atoms with CN = 9, 8 and 7, respectively. No energy correction was applied to Co atoms with CN = 11 and 12, as they were assumed to be inaccessible to CO. Co atoms with CN = 10 are mostly found at the base of B5-A step sites, that, as shown by Banerjee *et al.*,[20,21] are stabilized by C insertion in their fourfold interstice. Thus, by calculating the Gibbs free energy of reaction ($\Delta G_{rxn}$) at 500 K of:

$$Co_4^{B5\text{-}A} + CO + H_2 \rightarrow Co_4^{B5\text{-}A}C^{ins} + H_2O \quad (1)$$

where $Co_4^{B5\text{-}A}$ is the fourfold interstice in the B5-A site and $C^{ins}$ is the inserted carbon, and, considering that insertion does not occur in adjacent sites, the applied correction for CN = 10 was set as $\Delta G_{rxn}/2$. It is worth noting that this correction is the only one that will also depend on $p_{H_2O}/p_{H_2}$. The CO-covered (311) surface was chosen to model the B5-A sites. Furthermore, to model Co atoms with CN = 5 and 6, we removed some Co step atoms from the same surface to form triangular and hexagonal corners. Finally, a fixed correction of −0.6 eV was assigned to Co atoms with CN = 1, 2, 3 and 4,

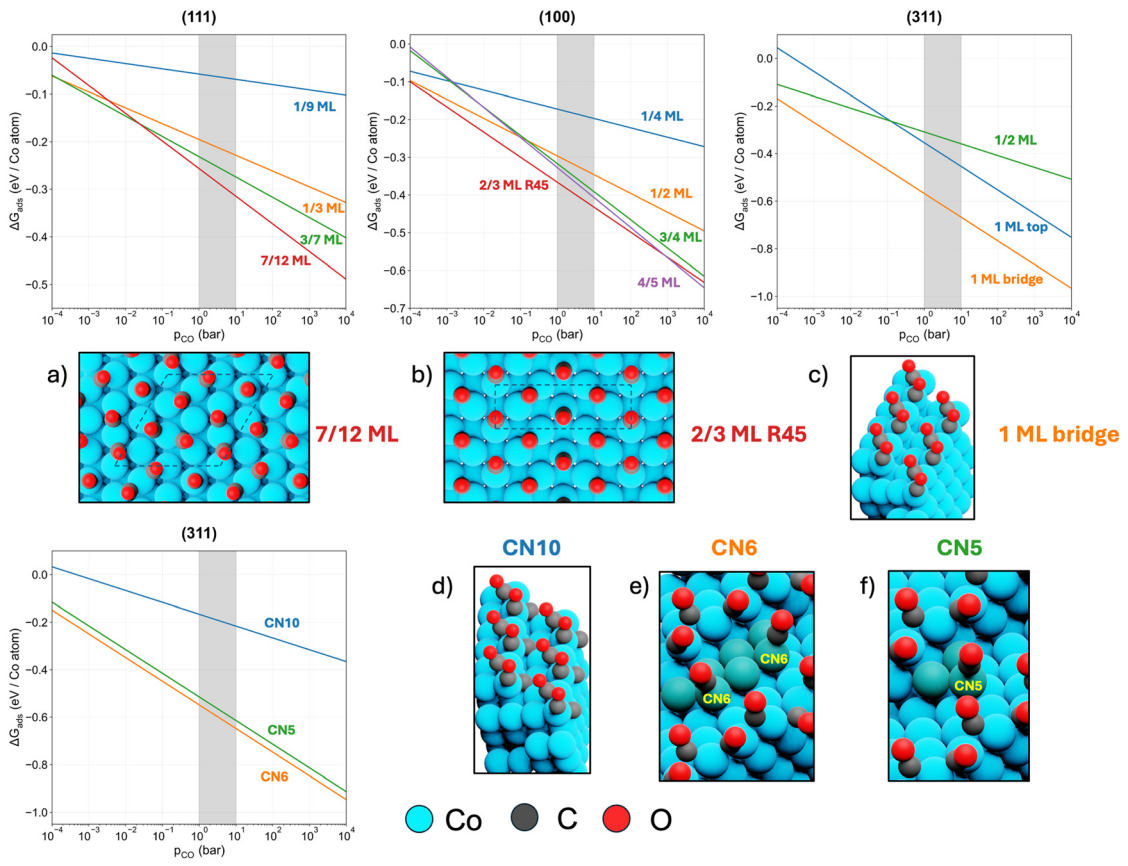


**Fig. 1** Phase diagrams at 500 K of CO coverages on different Co surfaces and most stable arrangements under relevant FT conditions of a) (111), b) (100) and c) (311) fcc Co facets (all other structures are shown in Fig. S2). Configurations used to calculate $\Delta G_{ads}$ for Co atoms with CN = 10, 6 and 5 are shown in d), e) and f), respectively. Turquoise Co atoms in e) and f) constitute the hexagonal and triangular corners. Shaded areas in the plot roughly indicate the $p_{CO}$ range under industrial FT conditions.

as they are not expected to be present in the final NPs structure even though they will appear throughout the execution of the algorithm. The phase diagrams of CO adsorption at 500 K on the different Co facets as well as snapshots of the most stable surface arrangements under typical FT conditions are shown in Fig. 1. Regarding the (111) surface, our results are in qualitative agreement with those reported by Gunasooriya *et al.*,[39] as we observe the same transitions from 1/3 ML to 3/7 ML and from 3/7 ML to 7/12 ML, even though we predict them to be shifted towards lower $p_{CO}$. Additionally, Weststrate *et al.*[40] indicated, on the grounds of predictions based on experimental measurements, that under FT conditions the equilibrium coverage for the hcp Co (0001) surface, analogous to fcc Co (111), would be approximately 0.5 ML, close to the 7/12 ML predicted from our calculations. In this arrangement, one CO occupies a top position and the remaining six occupy bridge positions in the unit cell. To further validate the accuracy of our computational approach to predict CO adsorption energies on Co, we calculated the low-coverage (1/9 ML, with CO in a top position) heat of adsorption (including ZPE contributions) of CO on Co (111) and obtained a value of −135 kJ mol$^{-1}$ (−1.41 eV), which is close to the experimental value of −128 kJ mol$^{-1}$ reported by Papp[41] for the analogous hcp (0001) surface. On the (100) surface, we report a slightly higher equilibrium coverage equal to 2/3 ML, where CO molecules are equally split between top and bridge positions. A significantly higher coverage of 1 ML is found on the (311) surface, where the bridge sites are preferred over the top ones as the former allow the CO molecules to be oriented in an alternating pattern, with consequent reduction of lateral interactions. We note that this arrangement has been reported experimentally for the stepped hcp Co (10–10) facet.[42] Table S2 shows $E_{Co}$ and $\Delta G_{ads}$ of CO normalized per Co atom with changing CN. The employed energy corrections for Co atoms with CN = 7, 8 and 9 are obtained by considering the identified most stable CO surface phases (*i.e.* the 7/12 ML, 2/3 ML R45 and 1 ML bridge, for the (111), (100) and (311) surfaces respectively) under FT conditions on the different surfaces shown in Fig. 1a–c, and by dividing the overall $\Delta G_{ads}$ of the stable phase by the number of (step, for the (311) facet) surface atoms in the unit cell. Thus, the employed energy corrections are the average $\Delta G_{ads}$ normalized to surface atoms, that for Co atoms with CN = 8 and 9 include the contribution from different CO binding modes (top and bridge) which are not considered explicitly during the MC runs. For CN = 5 and 6, only one CO surface phase corresponding to CO adsorbing on top of the corner atoms was considered.

As expected, in the CN range 7–10 the binding strength of CO increases with decreasing CN. We note that CO has been previously reported to bind more strongly to more open surfaces and thus to lower coordinated Co atoms.[41,43–45] Interestingly, $\Delta G_{ads}$ is shown not to increase further for CN = 6 and 5. The C insertion in the B5-A site induces a stabilization of Co atoms with CN = 10, even though to a lower extent compared to CO adsorption on Co atoms with lower CN. This stabilization is the most sensitive to $X_{CO}$, as it increases by about 60% upon switching from the high to the low $X_{CO}$ scenario. The calculated $\Delta G_{ads}$ of CO were included into the energy scheme presented in Fig. 2, that was employed in our MC algorithm to produce the structural models of Co NPs.

Under operating conditions, CO will not be the only adsorbate, since H and a number of reaction intermediates will cover the catalyst surface. Nonetheless, CO is the most strongly adsorbing species in the system, and it is thus expected to be predominant on the NPs surface. This is confirmed by a recent work by Rommens *et al.*,[46] where it was predicted that at FT conditions, of the total Co terraces coverage of 58.3%, 53.5% consists of CO and only the small remaining 4.8% of H and all other reaction intermediates. Thus, CO and the inserted C in the B5-A sites are the only adsorbates with high influence on catalyst structure, and hence only these are considered in this study.

We note that, by constraining the Co atoms into a fixed fcc grid, the hereby used lattice model is not suited to capture the local strain on the NPs surface and the consequent reconstruction it might induce, as well as amorphous bulk domains or surface sites. Additionally, by considering an ideal crystal lattice, our approach cannot reproduce symmetry-related irregularities such as stacking faults or mixed domains within particles. We further note that, since the CN specific energy corrections used to model the influence of CO adsorption are extrapolated from DFT calculations on periodic surface models, they can be transferred to the various facets of the nanoparticles but might fail to accurately describe CO adsorption and lateral interactions in proximity of the intersections between the facets, particularly when these are highly irregular. Nevertheless, we do not expect the overall metal–adsorbate

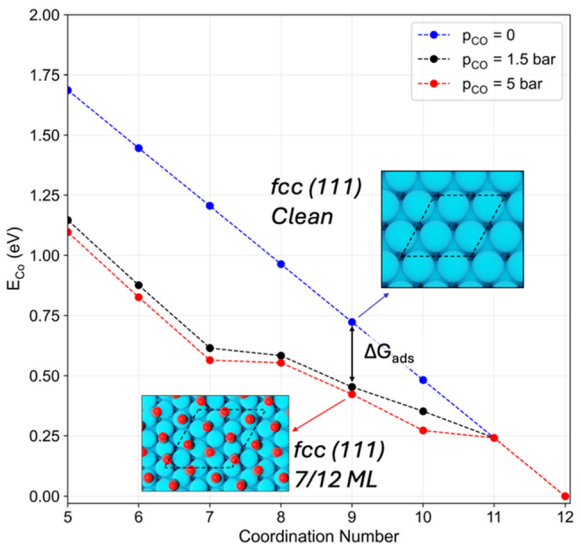


Fig. 2 $E_{Co}$ scaling with CN with increasing $p_{CO}$.

interactions on the facets intersections to significantly deviate from those on the extended surfaces, as Co atoms with same CN likely generate similar configurations of CO adsorption. We further note that the implicit modeling of CO during the MC runs leads to fixed energy corrections that include coverage-dependent effects implicitly at three fixed values of $p_{CO}$ = 0, 1.5 and 5 bar, that lead to just one most stable coverage on each facet in each scenario. This assumption is in line with the phase diagrams in Fig. 1, that show that, on each facet and within oscillations of $p_{CO}$ that can be expected under industrial FT conditions, only one coverage turns out to be the most stable, and thus energetic effects on NP stability deriving from surface coverage changes are likely not relevant. A further limitation of the implicit modeling of CO is that it does not capture adsorbate mobility. Nevertheless, our focus here is on equilibrium morphologies under representative CO coverages rather than on dynamic adsorbate rearrangements.

In Table 1 we additionally report the CO stretching frequencies for the 15 structures considered in this study. For each CO position, we obtain a range of frequencies depending on Co surface and coverage that are 1970–2023 $cm^{-1}$, 1870–1920 $cm^{-1}$ and 1768–1788 $cm^{-1}$ for top, bridge and hollow positions, respectively. These ranges are in good agreement with experimentally assigned IR peaks,[2,40,47] with the exception of the hollow sites that are underestimated by roughly 30 $cm^{-1}$. We further observe, in agreement with experiments,[40,47] that increasing surface coverage leads to a blue shift in the CO stretching frequencies, which indicates a strengthening of the C–O bond due to reduced backdonation from Co; this corroborates the idea that increasing coverage is detrimental to CO activation.[48] Interestingly, on the (111) and (100) facets the CO stretching frequencies start to increase only from 3/7 and 2/3 ML, respectively, suggesting that lateral interactions are negligible for the lower coverages.

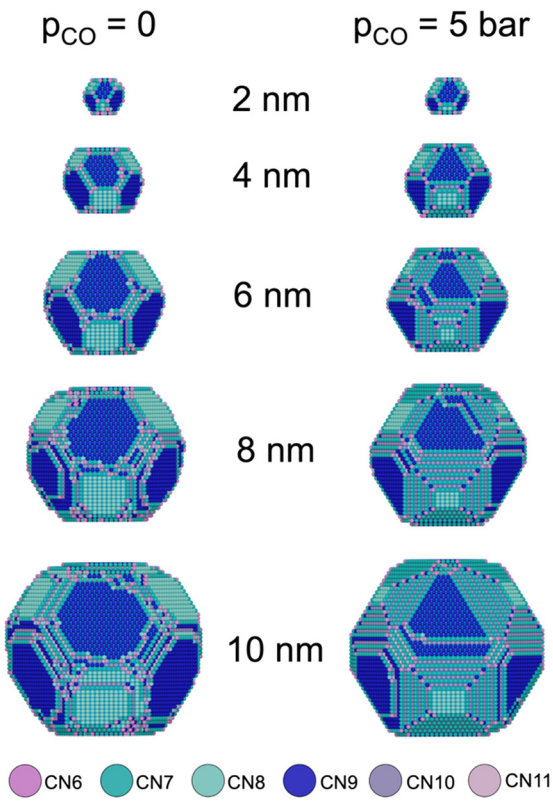


Fig. 3 Structural models of Co NPs in the investigated size range in vacuum and exposed to $p_{CO}$ = 5 bar.

### Structural characterization of Co NPs in CO atmosphere

The outcomes of the MC simulations are shown as snapshots of pristine and reconstructed Co NPs upon exposure to a gas phase of $p_{CO}$ = 5 bar, corresponding to the low $X_{CO}$ scenario, in Fig. 3. More snapshots of free standing and supported NPs in vacuum, in the high and low $X_{CO}$ scenarios are given in section S5. All reconstructed particles (except the 2 nm one) have a cuboctahedral shape, where semi-triangular (111)

Table 1 CO stretching frequencies on different Co facets at the different coverages considered in this study. These were calculated considering each CO molecule in the unit cell individually, *i.e.* by freezing all the atoms except one CO molecule. We employed a scaling factor of 1.008 for all the computed frequencies, that was chosen *ad hoc* to match the experimental CO stretching frequency in the gas phase of 2143 $cm^{-1}$. For the inserted C in the fourfold sites of the (311) facet, all three identified normal modes are reported

| | Top ($cm^{-1}$) | Bridge ($cm^{-1}$) | Hollow ($cm^{-1}$) | Inserted C ($cm^{-1}$) |
|---|---|---|---|---|
| (111) – 1/9 ML | 1973 | — | — | — |
| (111) – 1/3 ML | 1970, 1970, 1970 | — | — | — |
| (111) – 3/7 ML | 2002 | — | 1768, 1788 | — |
| (111) – 7/12 ML | 2015 | 1852, 1853, 1853, 1855, 1855, 1856 | — | — |
| (100) – 1/4 ML | 1985 | — | — | — |
| (100) – 1/2 ML | 1984, 1985 | — | — | — |
| (100) – 2/3 ML R45 | 1991 | — | — | — |
| (100) – 3/4 ML | 2003, 2003, 2007, 2007 | 1879, 1880 | — | — |
| (100) – 4/5 ML | 2009, 2012, 2023, 2024 | 1886, 1887, 1899, 1904 | — | — |
| (311) – 1/2 ML CO | 2003 | — | — | — |
| (311) – 1 ML CO Top | 1987, 2013 | — | | — |
| (311) – 1 ML CO Bridge | — | 1895, 1920 | — | — |
| (311) – 1 ML CO Bridge + 0.5 ML C | — | 1904, 1928 | — | 703–612–386 |
| CN6 | 1989, 1994 | — | — | — |
| CN5 | 2016 | — | — | — |

terraces alternate with extended square surfaces mostly occupied by (311)-like regions exposing B5-A step sites and culminating with small (100) regions. The (110) surfaces composed of B5-B sites are found at the (111)/(111) intersections. With growing size, the surfaces of both the pristine and reconstructed particles become increasingly irregular (*i.e.* defective), even though this is more prominent for the former. We have discussed the increase of surface defects with growing particle size in light of the configurational entropy contribution to NP stability in our previous work, which has been largely in line with outcomes of other models for Co particles.[13,14,16]

The effect of the gas phase on the NPs shapes is further highlighted in Fig. 4, where we present snapshots of $CoTiO_3$-supported 8 nm Co NPs for different values of $p_{CO}$. Note that the interaction between Co and $CoTiO_3$ has been calculated as −103 meV Å$^{-2}$ in our earlier work, where we also discuss the effect of adhesion interactions on the overall particle shape. With increasing $p_{CO}$, the NPs gradually transition from the truncated octahedron to the cuboctahedron morphology, as the (100) surfaces shrink in favor of (311) regions and the (111) terraces evolve from the hexagonal to the triangular shape. The formation of triangular (111) terraces is primarily driven by carbon insertion into the fourfold interstice at the B5-A sites, which stabilizes them more than their B5-B counterparts. This results in the three alternating sides of the hexagonal terraces found at the (100)/(111) intersections (where the B5-A sites are present) to grow at the expenses of the remaining three corresponding to the (111)/(111) intersections, thus causing the observed shift towards a triangular conformation. Previous experimental works have observed triangular nano-islands formation over Co single crystals upon exposure to a syngas mixture[19,21] and to pure CO.[49] Furthermore, theoretical calculations by Banerjee *et al.*[20] predicted spontaneous formation of these structures on (111) planes under FT conditions, for which, they argued, C insertion plays a decisive role.

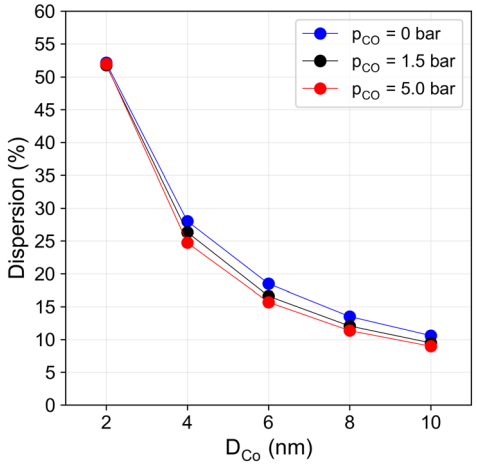


Fig. 5 Dispersion (defined as $N_{surf}/N_{tot}$ where $N_{tot}$ and $N_{surf}$ are the total number of atoms and number of surface atoms, respectively) of free-standing Co NPs with increasing $D_{Co}$ and $p_{CO}$. Error bars have been omitted as they are negligibly small.

From the side view of Fig. 4, we additionally observe that exposure to the gas phase triggers a transition from a highly faceted NP shape to a rounder one. As shown in Fig. 5, this results in lower Co dispersion, since this change of morphology ensures a lower surface to volume ratio. We note that a similar shape evolution has been previously reported for Pt nanoparticles in CO atmosphere.[50,51]

Fig. 4 also illustrates the impact of CO on the MSI. As $p_{CO}$ increases, the effective $\gamma_{adh}$ decreases, leading to less flattening of the NPs on the support. On the strongly interacting $CoTiO_3$ support, the nanoparticles reach heights of 25, 27, and 28 atomic layers in vacuum, at low $X_{CO}$ and high $X_{CO}$, respectively. Our calculations predicted that $\gamma_{adh}$ on $SiO_2$ would be lower than $\Delta G_{ads}$(111) in both

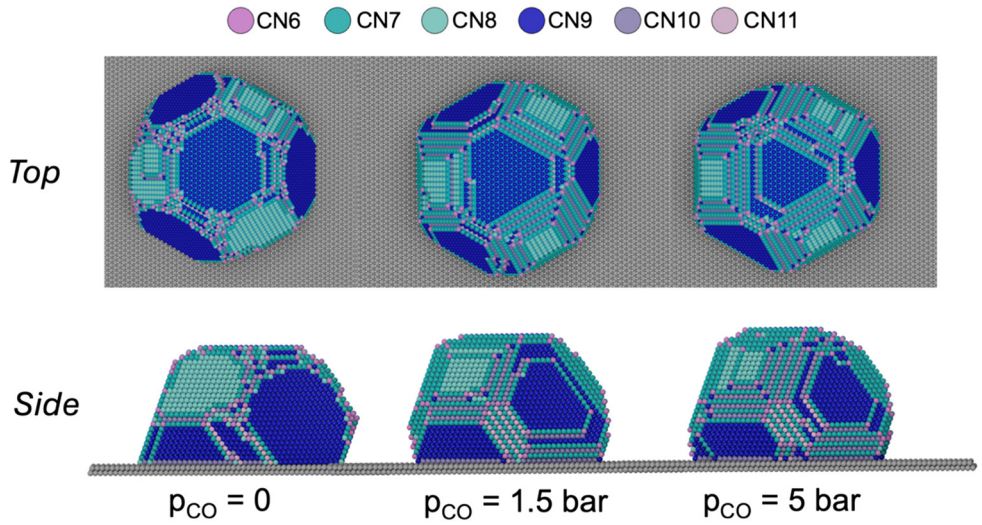


Fig. 4 Top and side views of a $CoTiO_3$-supported 8 nm Co NP in vacuum, in the high $X_{CO}$ ($p_{CO}$ = 1.5 bar) and low $X_{CO}$ ($p_{CO}$ = 5 bar) scenarios. Co atoms are colored based on their coordination number.

the high and low $X_{CO}$ scenarios, thus causing complete detachment of the NPs from the support. We are not aware of studies reporting leaching of Co NPs in $SiO_2$-supported catalysts, suggesting that either our models did not capture the real conformation of the Co–$SiO_2$ interface, and that the actual one guarantees stronger Co–support interactions, or that leaching is kinetically hindered. At any rate, this study shows that CO will likely enhance mobility of the NPs by reducing their interactions with the support and might hence contribute to particle migration and coalescence.

The surface reconstruction induced by CO is quantified *via* the site distribution analysis shown in Fig. 6. The most evident effect of CO is a decrease of 2B3 and B4 sites against a dramatic increase of B5-A sites, resulting from the observed shrinking of the close-packed (111) and (100) surfaces in favor of (311) regions. B5-B sites are shown to slightly decrease while B6 sites almost disappear upon surface reconstruction, despite increasing with NP size. The only exception is the 2 nm NP, that displays a certain inertia against exposure to CO, indicating that small NPs might be less sensitive to surface reconstruction. For these particles, in fact, we observe only a minor increase of B4 sites at the expenses of 2B3 sites upon CO adsorption. It is also worth noting that fluctuations of $p_{CO}$ that are within the expected range of FT operation significantly affect surface reconstruction. For the 10 nm NP, in fact, we report a 4.6%, 4.9% and 11.4% differences for the 2B3, B4 and B5-A site percentages, respectively, between the high and low $X_{CO}$ scenarios. As for the particles in vacuum, different supports were shown not to influence the site distribution to a significant extent, as shown in Section S6.

We note that the observed increase in B5-A step sites upon surface reconstruction is directly linked to the energy correction used in the model to describe Co atoms with CN = 10. Nonetheless, the inclusion of this correction is not an arbitrary choice, as DFT calculations show that C insertion is indeed thermodynamically favorable. The fact that this energy gain has such a drastic impact on NPs morphology is an original conclusion of this work that could not be expected *a priori* just based on the model setup. Furthermore, to assess the sensitivity of the model on this effect, we carried out three more sets of MC runs for free-standing particles in the low $X_{CO}$ scenario, where, instead of using the energy correction for CN10 obtained from the calculated $\Delta G_{rxn}$ = 0.42 eV from eqn (1), we considered $\Delta G_{rxn}$ = 0.32, 0.21 (*i.e.*, $\frac{3}{4}$ and $\frac{1}{2}$ of the original correction) and 0 eV. The results of this analysis, presented in Fig. S3, show that, without considering C insertion in the B5-A sites, Co NPs undergo a different type of surface reconstruction as B5-A sites mostly disappear in favor of B4 and B5-B sites. On the other hand, considering $\Delta G_{rxn}$ = 0.32 and 0.21 eV leads to a qualitatively similar reconstruction as compared to the original case of $\Delta G_{rxn}$ = 0.42 eV, as in both cases we witness an increase of B5-A sites % with respect to the particles in vacuum. Nonetheless, the magnitude of the reconstruction changes significantly with $\Delta G_{rxn}$, as the B5-A sites % peak for the 10 nm NPs at 12.7, 26.7 and 37.3%, considering $\frac{1}{2}$, $\frac{3}{4}$ and the full CN10 correction, respectively, as compared to 7.8% for the particles in vacuum. These results underscore that, while the model is rather sensitive to the magnitude of the correction for CN10,

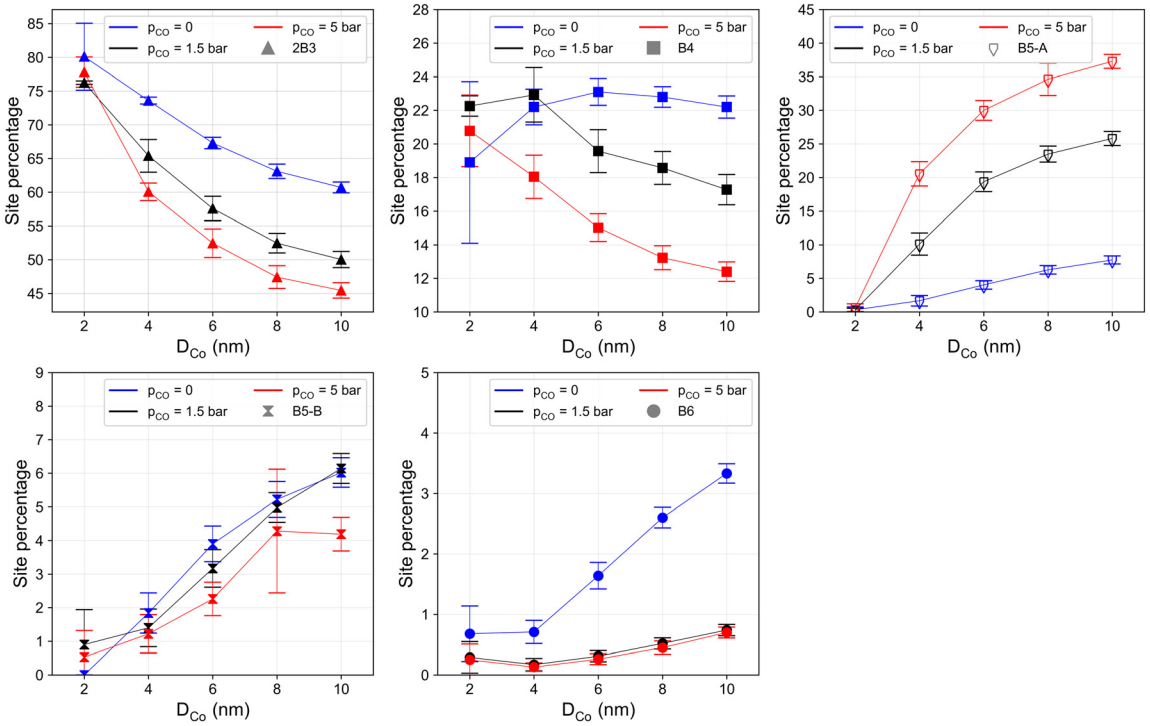


**Fig. 6** Site distribution analysis with increasing particle size and changing $p_{CO}$.

the CO-induced surface reconstruction is qualitatively reproduced within reasonable deviations of $\Delta G_{rxn}$.

The observed changes in site distribution suggest that CO-induced surface reconstruction might significantly affect FT activity. Raltson *et al.*[52] demonstrated that the increased activity on larger NPs was associated with greater coverage of C monomers, suggesting that they catalyze CO splitting more effectively. Moreover, previous studies[3,4] have shown that the activation energy of the reaction remains constant with changing NP size, indicating that the size dependency of the TOF does not originate from the appearance of alternative reaction paths and/or other Co surfaces. The combination of these information hints at the fact that the structure sensitivity of Co catalysts arises from the larger number of CO-splitting sites on bigger NPs, as it has been previously postulated.[13–15] Theoretical calculations have shown that the B5-A sites can directly dissociate CO, with reaction barriers that are in reasonable agreement with the experimentally observed activation energy.[53,54] Considering the representative high $X_{CO}$ scenario corresponding to $p_{CO}$ = 1.5 bar, we note that B5-A sites increase linearly up to 6 nm, after which they start approaching a plateau. This resembles the reported TOF dependence on particle size, that increases linearly up to 10 nm and stays constant afterwards. B5-A sites might hence largely contribute to CO activation during FT. If this is indeed the case, our calculations indicate that surface reconstruction would be beneficial for activity as it drastically increases the B5-A sites concentration, a hypothesis put forward in previous experimental studies.[55,56] It has frequently been reported that Co catalysts undergo an induction period in the initial stage of the FT synthesis, during which the activity increases until it reaches a maximum, and later stabilizes at steady-state regime.[55,57–59] This has often been interpreted as the time necessary for the NPs surface to reconstruct and expose more active sites. Fischer *et al.*[5] investigated the effect of Co exposure to CO by pretreating the catalyst in a pure CO atmosphere and testing its performance. They observed lower activity of the pretreated catalyst with respect to the pristine one, and hence they concluded that surface reconstruction had induced deactivation. We speculate that the pretreatment might have induced detrimental reconstruction due to the lack of $H_2$. In its absence, in fact, the C monomers formed upon CO splitting cannot be hydrogenated and product desorption will be inhibited. Hence, carbon might couple to form oligomeric and graphitic species that will cover the active sites, and/or might diffuse into the catalyst surface and cause reconstruction of the (111) and (100) terraces, or deeper into the bulk to form $Co_2C$.[60–63] These are common causes of catalyst deactivation[64] and can explain the effect of the pretreatment. Thus, we postulate that beneficial surface reconstruction can take place if conditions of depleted $H_2$ are avoided.

B5-B sites could also contribute to CO splitting as they increase linearly with NP size, even though they approach a plateau around 8–10 nm only for the unsupported particles, and possibly because of the high uncertainty of the data point corresponding to their concentration at $D_{Co}$ = 8 nm. Furthermore, B5-B sites, found on the (110) and (221) surfaces, are predicted to be less active for direct CO splitting than B5-A ones.[65] Liu *et al.*[66] reached the opposite conclusion, but likely because they did not identify the most stable transition state (TS) on the (311) surface,[65] in which the carbon atom is inserted in the fourfold site at the base of the step-edge rather than on the threefold one below it. Furthermore, CO dissociation on Ru was shown to occur preferentially on B5-A rather than B5-B steps.[67] Interestingly, our results hint at a limited role of B6 sites in the FT reaction given their extremely low presence on the reconstructed NP surface, despite the calculated CO splitting barrier on this configuration being lower than on conventional step sites.[65] On the other hand, the activation energy of the FT synthesis on fcc Co was experimentally determined to be 144 kJ $mol^{-1}$,[68] significantly larger than the predicted one for CO dissociation on kink sites at low coverages. This indicates that, despite being in principle more active, B6 sites might not be available during the reaction, in line with the results presented in this work.

The predicted impact of CO induced surface reconstruction on catalyst performance has been rationalized based on previous experimental as well as theoretical kinetic studies, that revealed the importance of step sites for the FT synthesis on Co.[14,46,69–73] However, the performance trends discussed here are more of a qualitative nature, and future works could take the calculated surface sites and corresponding CO coverages into account to develop more in-depth multi-site kinetic models.[74]

We note that contradicting reports exist about the magnitude of CO-induced surface reconstruction of Co. Among the studies that achieved atomic resolution of Co single crystal surfaces,[19,21,23,72,75] some observed marked surface reconstruction upon syngas exposure, while others yielded opposite results. This might be motivated by the lower pressures employed in these latter works, as Ehrensperger *et al.*[75] and Böller *et al.*[72] conducted their experiments at a syngas pressure of 50 and 950 mbar, respectively, which may be too low to observe significant surface rearrangement. Additionally, these studies considered Co (0001) single crystals, which might behave differently from Co NPs. Indications of surface reconstruction of Co NPs during FT were obtained by Bezemer *et al.*,[1] that reported a reduction of Co atoms CN as measured by EXAFS following catalytic testing, which is in line with the increase in lower coordinated sites upon surface reconstruction predicted in this study. An *in situ* FTIR study by Prieto *et al.*[22] provides further evidence of surface reconstruction of Co NPs during FT. In fact, the appearance of peaks relative to C–O stretching frequencies located at lower bands during FT testing, that was attributed to CO binding to lower-coordinated Co atoms, suggested that significant surface reconstruction had taken place. Interestingly, these peaks appeared concomitantly with others located at lower frequencies and assigned to adsorbed C atoms, that were hence speculated to have

 

induced the reconstruction. Some of these species might have been C atoms inserted in the B5-A sites fourfold interstices, which we have shown to significantly influence the morphological transformation. We point out that previous theoretical studies[24–26] that have modelled Co NPs in a CO environment have reported that CO would shrink the stepped surfaces in favor of the close-packed (111) facet. One reason for the discrepancy with our results might be that these works employed the classical Wulff construction to build their models, whose limitations we have highlighted in our previous work. Another is that none of these studies included C insertion in the B5-A sites when modelling CO adsorption. Moreover, the idea that NPs develop higher faceting upon exposure to CO appears to contradict experimental evidence, which instead suggests surface corrugation.

Despite having been proposed decades ago, the CO induced surface reconstruction of Co catalysts is still heavily debated. This is partially due to the difficulty of obtaining experimental evidence that can unambiguously prove the occurrence of this phenomenon under industrial FT conditions, where the high pressures and the extensive production of wax make the application of several experimental techniques not a trivial task. In this context, we believe that approaching the problem from the theoretical perspective can be helpful, since it offers the benefit of decoupling the impact of several factors and ultimately yields a simplified description of an otherwise complex chemical system.

### Stability and surface energies of Co NPs in CO atmosphere

Besides influencing the structures of Co NPs, the interaction with CO (*e.g.* during FT synthesis) will also affect their stability. This is shown in Fig. 7, where we report the $\gamma$, average energy per atom ($\Delta E_{Co}$) and chemical potential ($\Delta\mu_{Co}$) of the free-standing Co NPs with increasing $p_{CO}$. The results for the supported particles are given in section S7. Despite provoking the exposure of a larger number of low-coordinated sites as shown in section 3.2, CO causes a drastic reduction of $\gamma$ of roughly 40% and 45% for $p_{CO}$ = 1.5 and 5 bar, respectively. This might explain the observation by several experimental studies[76–80] of further reduction of Co catalysts when put in operation after the activation stage. In fact, the persistence of Co(II)O after reduction can be ascribed to its lower $\gamma$ with respect to metallic Co. This highlights that the reduction of small particles, for which the effect of $\gamma$ on the stability is large, is less favourable due to the higher surface energy of $Co^0$, as shown in earlier work, both for Co[81] as well as for other metals such as Ni.[82] Interestingly, small particles that did not reduce during activation, might do so when exposed to the FT gas-phase considering the drastic reduction of $\gamma$ that is calculated for the case of CO adsorption. Additionally, we note that the decrease of $\gamma$ with

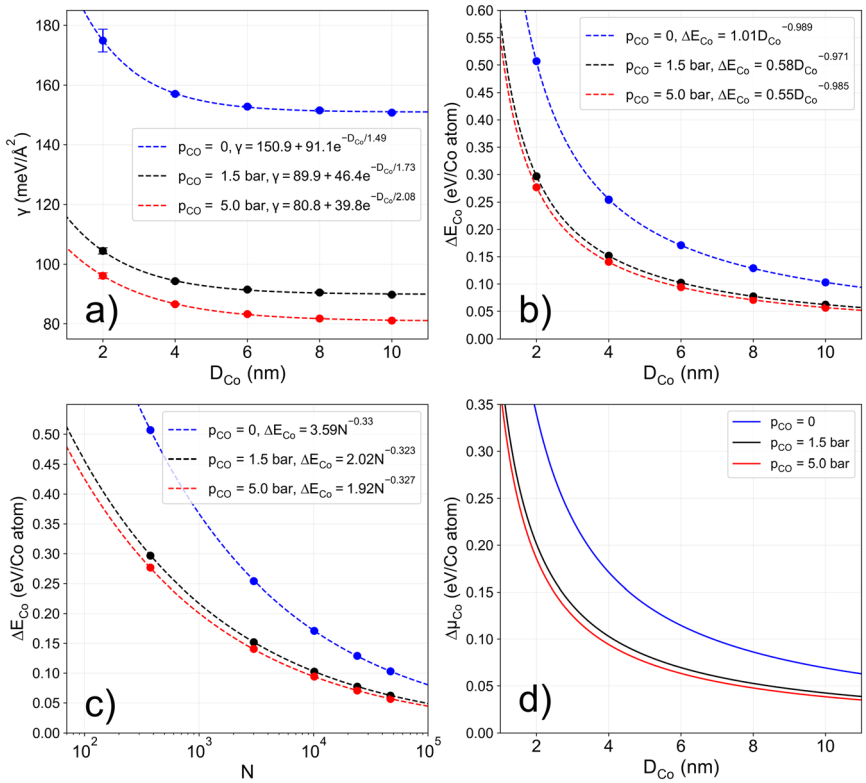


**Fig. 7** Free-standing Co NPs a) surface energies with increasing $D_{Co}$ and $p_{CO}$, b) average energy per atom $\Delta E_{Co}$ with respect to bulk Co with increasing $D_{Co}$ and $p_{CO}$ and c) with increasing number of atoms (N) and $p_{CO}$. d) Chemical potential of the free-standing Co NPs in respect to bulk Co $\Delta\mu_{Co}$ with increasing $D_{Co}$ and $p_{CO}$.

$D_{Co}$ due to decreasing concentration of low-coordinated atoms is less significant in the CO atmosphere since, for $p_{CO}$ = 1.5 and 5 bar, $\gamma$ decreases by ~15 meV Å$^{-2}$ between the 2 and the 10 nm particles, while it does so by 24 meV Å$^{-2}$ in the absence of CO.

As shown in Fig. 7b, increasing $p_{CO}$ also lowers $\Delta E_{Co}$, an effect that we ascribe to two factors. On the one hand, as shown in Fig. 7a, CO exposure lowers the $\gamma$ of Co NPs. On the other hand, Co NPs in CO atmosphere are characterized by a lower surface/volume ratio, as shown in the plot of the dispersion against $D_{Co}$ in Fig. 5, since the corrugation of the surface makes them assume a rounder shape. We additionally note that the dependence of $\Delta E_{Co}$ on $p_{CO}$ is not linear, since increasing $p_{CO}$ from 0 to 1.5 bar causes a marked drop of $\Delta E_{Co}$, while a further increase to $p_{CO}$ = 5 bar results in only a marginal decrease. This stems from the dependence of $\Delta G_{ads}$ on the logarithm of $p_{CO}$, that causes a rather slow change of $\Delta E_{Co}$ in respect to the variations of $p_{CO}$ that can be expected during the FT synthesis. Thus, we conclude that, during operation, the overall thermodynamic stability of Co NPs will not be significantly affected by fluctuations of $p_{CO}$ in the 1–10 bar range.

We additionally evaluated $\Delta\mu_{Co}$, which is reported in Fig. 7d, according to the following equation:[83]

$$\Delta\mu_{Co} = \left(\frac{\partial(N \times \Delta E_{Co})}{\partial N}\right)_{T,p} \quad (2)$$

The above derivative was taken by substituting $\Delta E_{Co}(N)$ with the fitting functions reported in Fig. 7c.

The considerations made for $\Delta E_{Co}$ are also valid for $\Delta\mu_{Co}$. We observe that the curves of $\Delta\mu_{Co}$ become significantly less steep upon exposure to CO, since the $\Delta\mu_{Co}$ decrease with $D_{Co}$ in the 2–10 nm size range is ~0.16 eV per atom in the presence of CO while it is 0.29 eV per atom for particles in vacuum. Since CO mainly impacts the stability of the NPs by lowering their surface energy, it stabilizes smaller particles to a larger extent than bigger ones as the former have a larger surface/volume ratio. Hence, CO reduces the thermodynamic driving force for sintering of Co NPs. Importantly, however, the presence of CO will significantly increase the kinetics of sintering. We have shown in section 3.2 that CO lowers the adhesion energy of Co NPs on the support, causing them to migrate and coalesce more easily. Furthermore, increasing $p_{CO}$ favors the formation of Co subcarbonyl species thought to be responsible for sintering through Ostwald ripening.[84–87] Extensive experimental characterization of $\gamma$-$Al_2O_3$ – supported Co catalysts under operation has shown that increasing $p_{CO}$ enhances sintering,[85] suggesting that the increase in sintering kinetics alleviates the decrease of the thermodynamic driving force.

Overall, by considering the case study of CO adsorption on Co NPs, this section shows that the gas phase to which metal NPs are exposed may have considerable effects on their stability, underscoring that the modelling of phenomena that depend on this property (such as sintering, metal reoxidation and encapsulation by the support) should not neglect the impact of adsorbates, which we can elegantly include within the framework of our DFT-MC model.

# Conclusions

We have expanded the paired DFT-MC approach for metal NPs modelling introduced in our previous work to take the Co–CO interactions into account. We derived CN-specific energy corrections for Co atoms based on CO $\Delta G_{ads}$ on low-index fcc facets and included these values in our energy model accordingly, thus accounting for this important factor in a straightforward manner.

We found that CO adsorption profoundly alters Co NPs structures, triggering effects that are expected to have a large impact on overall catalysts performance. The dramatic increase of B5-A sites, on which CO can be dissociated, corroborates the idea proposed in previous studies that surface reconstruction enhances catalyst activity. A further indication that B5-A sites play an important role in the reaction is that the evolution of their concentration with particle size under typical FT conditions somewhat mirrors the reported size-dependent behavior of the TOF of Co catalysts. B5-B sites might also contribute to catalyst activity, even though their concentration is hardly affected by Co–CO interactions. B6 sites, that were predicted to be the most active for CO splitting, almost disappear upon surface reconstruction, suggesting that their relevance in the reaction network is marginal.

The impact of CO on NPs stability was found to be significant. The drastic reduction of the surface energy of Co NPs upon CO adsorption likely affects both their redox behavior and their resistance to sintering, whose thermodynamic driving force is considerably lowered by exposure to CO. This thermodynamic effect, however, is presumably overshadowed by the positive impact that CO has on the kinetics of the process, since it is speculated to trigger the formation of Co subcarbonyl species that are responsible for sintering *via* Ostwald ripening.

In conclusion, strongly adsorbing molecules like CO can have a drastic impact on metal NPs structures and stability, which are fundamental aspects determining the catalytic performance. Nonetheless, providing models that take this effect into account without neglecting other important aspects such as particles size and metal–support interactions has proven challenging, mostly due to the limitations of the classical techniques to model metal NPs. With the present approach, we were able to obtain, with only a handful of DFT calculations, an in-depth description of Co NPs under operating conditions where all parameters are obtained exclusively from first-principles calculations. Importantly, this strategy can be readily applied to other catalytic systems, anticipating great potential for future applications.

 

## Author contributions

Enrico Sireci: conceptualization, data curation, formal analysis, investigation, methodology, validation, visualization, writing – original draft, writing – review & editing. Tilman D. Grüger: conceptualization, data curation, formal analysis, methodology, software, validation. Philipp N. Plessow: conceptualization, methodology, software, supervision. Dmitry I. Sharapa: conceptualization, data curation, supervision, writing – review & editing. Felix Studt: conceptualization, funding acquisition, methodology, project administration, resources, supervision, writing – review & editing.

## Conflicts of interest

There are no conflicts to declare.

## Data availability

Supplementary information: coordinates in xyz format and potential energies of all DFT-calculated structures are provided separately (TXT). Additional data supporting this article have also been included (PDF). See DOI: **https://doi.org/10.1039/d5cy00921a**.

Home-made Monte Carlo code MC-Cluster available at **https://github.com/T-136/MC-Cluster/tree/master** or **https://doi.org/10.35097/pqmqcrq4h47eucz5**.

Results of MC simulations (lowest energy geometries and energies, as well as energies and CN-profile taken every $5 \times 10^7$ iterations for each run) for all the investigated particles are available at the KITopen repository at **https://doi.org/10.35097/uc9rvb47cz9r04d3**.

## Acknowledgements

The authors gratefully acknowledge the financial support of the German Federal Ministry of Research, Technology and Space (BMFTR) within the CARE-O-SENE project (03SF0673). The authors acknowledge support by the state of Baden-Württemberg through bwHPC and the German Research Foundation (DFG) through grant no. INST 40/575-1 FUGG (JUSTUS 2 cluster, RVs bw17D011). Support from the Helmholtz Association is also gratefully acknowledged.

## Notes and references

1 G. L. Bezemer, J. H. Bitter, H. P. C. E. Kuipers, H. Oosterbeek, J. E. Holewijn, X. Xu, F. Kapteijn, A. J. Van Diilen and K. P. De Jong, *J. Am. Chem. Soc.*, 2006, **128**, 3956–3964.
2 G. Prieto, A. Martínez, P. Concepción and R. Moreno-Tost, *J. Catal.*, 2009, **266**, 129–144.
3 J. Yang, E. Z. Tveten, D. Chen and A. Holmen, *Langmuir*, 2010, **26**, 16558–16567.
4 T. Herranz, X. Deng, A. Cabot, J. Guo and M. Salmeron, *J. Phys. Chem. B*, 2009, **113**, 10721–10727.
5 N. Fischer, E. Van Steen and M. Claeys, *J. Catal.*, 2013, **299**, 67–80.
6 T. O. Eschemann, W. S. Lamme, R. L. Manchester, T. E. Parmentier, A. Cognigni, M. Rønning and K. P. De Jong, *J. Catal.*, 2015, **328**, 130–138.
7 G. Melaet, A. E. Lindeman and G. A. Somorjai, *Top. Catal.*, 2014, **57**, 500–507.
8 W. T. Ralston, G. Melaet, T. Saephan and G. A. Somorjai, *Angew. Chem.*, 2017, **129**, 7523–7527.
9 H. Xiong, M. A. M. Motchelaho, M. Moyo, L. L. Jewell and N. J. Coville, *J. Catal.*, 2011, **278**, 26–40.
10 K. T. Rommens and M. Saeys, *Chem. Rev.*, 2023, **123**, 5798–5858.
11 J. Van de Loosdrecht, F. G. Botes, I. M. Ciobîcă, A. Ferreira, P. Gibson, D. J. Moodley, A. M. Saib, J. L. Visagie, C. J. Weststrate and J. W. Niemantsverdriet, *Comprehensive Inorganic Chemistry II (Second Edition): From Elements to Applications*, 2013, vol. 7, pp. 525–557.
12 A. Tuxen, S. Carenco, M. Chintapalli, C. H. Chuang, C. Escudero, E. Pach, P. Jiang, F. Borondics, B. Beberwyck, A. P. Alivisatos, G. Thornton, W. F. Pong, J. Guo, R. Perez, F. Besenbacher and M. Salmeron, *J. Am. Chem. Soc.*, 2013, **135**, 2273–2278.
13 P. Van Helden, I. M. Ciobîcă and R. L. J. Coetzer, *Catal. Today*, 2016, **261**, 48–59.
14 M. P. C. Van Etten, B. Zijlstra, E. J. M. Hensen and I. A. W. Filot, *ACS Catal.*, 2021, **11**, 8484–8492.
15 M. P. C. Van Etten, M. E. De Laat, E. J. M. Hensen and I. A. W. Filot, *J. Phys. Chem. C*, 2023, **127**, 15148–15156.
16 R. Agrawal, P. Phatak and L. Spanu, *Catal. Today*, 2018, **312**, 174–180.
17 D. Moodley, J. Potgieter, P. Moodley, R. Crous, P. van Helden, L. van Zyl, R. Cunningham, J. Gauché, K. Visagie, T. Botha, M. Claeys and E. van Steen, *Catal. Today*, 2025, **454**, 115282.
18 E. Sireci, T. D. Grüger, P. N. Plessow, D. I. Sharapa and F. Studt, *J. Phys. Chem. C*, 2025, **129**(29), 13232–13243.
19 J. Wilson and C. De Groot, *J. Phys. Chem.*, 1995, **99**, 7860–7866.
20 A. Banerjee, A. P. Van Bavel, H. P. C. E. Kuipers and M. Saeys, *ACS Catal.*, 2015, **5**, 4756–4760.
21 A. Banerjee, V. Navarro, J. W. M. Frenken, A. P. Van Bavel, H. P. C. E. Kuipers and M. Saeys, *J. Phys. Chem. Lett.*, 2016, **7**, 1996–2001.
22 G. Prieto, A. Martínez, P. Concepción and R. Moreno-Tost, *J. Catal.*, 2009, **266**, 129–144.
23 V. Navarro, M. A. Van Spronsen and J. W. M. Frenken, *Nat. Chem.*, 2016, **8**, 929–934.
24 H. Lin, J. X. Liu, H. J. Fan and W. X. Li, *J. Phys. Chem. C*, 2020, **124**, 23200–23209.
25 J. E. De Vrieze, G. M. Bremmer, M. Aly, V. Navarro, J. W. Thybaut, P. J. Kooyman and M. Saeys, *ACS Catal.*, 2019, **9**, 7449–7456.
26 M. Yu, L. Liu, L. Jia, D. Li, Q. Wang and B. Hou, *Appl. Surf. Sci.*, 2020, **504**, 144469.

27 R. Cheula, M. Maestri and G. Mpourmpakis, *ACS Catal.*, 2020, **10**, 6149–6158.
28 G. Spanò, M. Ferri, R. Cheula, M. Monai, B. M. Weckhuysen and M. Maestri, *ACS Catal.*, 2025, 8194–8203.
29 E. M. Dietze, P. N. Plessow and F. Studt, *J. Phys. Chem. C*, 2019, **123**, 25464–25469.
30 P. J. Feibelman, B. Hammer, J. K. Norskov, F. Wagner, M. Scheffler, R. Stump, R. Watwe and J. Dumesic, *J. Phys. Chem. B*, 2001, **105**, 4018–4025.
31 L. Schimka, J. Harl, A. Stroppa, A. Grüneis, M. Marsman, F. Mittendorfer and G. Kresse, *Nat. Mater.*, 2010, **9**, 741–744.
32 J. Wellendorff, K. T. Lundgaard, A. Møgelhøj, V. Petzold, D. D. Landis, J. K. Nørskov, T. Bligaard and K. W. Jacobsen, *Phys. Rev. B: Condens. Matter Mater. Phys.*, 2012, **85**, 235149.
33 J. Wellendorff, T. L. Silbaugh, D. Garcia-Pintos, J. K. Nørskov, T. Bligaard, F. Studt and C. T. Campbell, *Surf. Sci.*, 2015, **640**, 36–44.
34 W. R. Tyson and W. A. Miller, *Surf. Sci.*, 1977, 267–276.
35 G. Kresse and J. Furthmüller, *Comput. Mater. Sci.*, 1996, **6**, 15–50.
36 G. Kresse and J. Hafner, *Phys. Rev. B: Condens. Matter Mater. Phys.*, 1993, **47**, 558–561.
37 G. Kresse and D. Joubert, *Phys. Rev. B: Condens. Matter Mater. Phys.*, 1999, **59**, 1758–1775.
38 R. van Hardeveld and F. Hartog, *Surf. Sci.*, 1969, **15**, 189–230.
39 G. T. K. K. Gunasooriya, A. P. Van Bavel, H. P. C. E. Kuipers and M. Saeys, *Surf. Sci.*, 2015, **642**, L6–L10.
40 C. J. Weststrate, J. van de Loosdrecht and J. W. Niemantsverdriet, *J. Catal.*, 2016, **342**, 1–16.
41 H. Papp, *Surf. Sci.*, 1983, **129**, 205–218.
42 R. L. Toomes and D. A. King, *Surf. Sci.*, 1996, **349**, 1–18.
43 K. Liao, V. Fiorin, D. S. D. Gunn, S. J. Jenkins and D. A. King, *Phys. Chem. Chem. Phys.*, 2013, **15**, 4059–4065.
44 H. Papp, *Surf. Sci.*, 1985, **149**, 460–470.
45 H. Papp, *Ber. Bunsenges. Phys. Chem.*, 1982, **86**, 555–562.
46 K. T. Rommens, G. T. K. K. Gunasooriya and M. Saeys, *ACS Catal.*, 2024, **14**, 6696–6709.
47 G. A. Beitel, A. Laskov, H. Oosterbeek and E. W. Kuipers, *J. Phys. Chem.*, 1996, 12494–12502.
48 W. Chen, I. A. W. Filot, R. Pestman and E. J. M. Hensen, *ACS Catal.*, 2017, **7**, 8061–8071.
49 B. Böller, M. Ehrensperger and J. Wintterlin, *ACS Catal.*, 2015, **5**, 6802–6806.
50 T. Avanesian, S. Dai, M. J. Kale, G. W. Graham, X. Pan and P. Christopher, *J. Am. Chem. Soc.*, 2017, **139**, 4551–4558.
51 H. Yoshida, K. Matsuura, Y. Kuwauchi, H. Kohno, S. Shimada, M. Haruta and S. Takeda, *Appl. Phys. Express*, 2011, **4**, 065001.
52 W. T. Ralston, G. Melaet, T. Saephan and G. A. Somorjai, *Angew. Chem.*, 2017, **129**, 7523–7527.
53 P. Van Helden, J. A. Van Den Berg and I. M. Ciobîcă, *Catal. Sci. Technol.*, 2012, **2**, 491–494.
54 A. Banerjee, A. P. Van Bavel, H. P. C. E. Kuipers and M. Saeys, *ACS Catal.*, 2017, **7**, 5289–5293.
55 K. F. Tan, J. Chang, A. Borgna and M. Saeys, *J. Catal.*, 2011, **280**, 50–59.
56 H. Schulz, Z. Nie and F. Ousmanov, *Catal. Today*, 2002, **71**, 351–360.
57 S. Bai, C. Huang, J. Lv and Z. Li, *Catal. Commun.*, 2012, **22**, 24–27.
58 M. Martinelli, M. Kumaran Gnanamani, S. D. Hopps, D. E. Sparks, A. MacLennan, Y. Hu, B. H. Davis and G. Jacobs, *ChemCatChem*, 2018, **10**, 3709–3716.
59 J. Il Yang, J. H. Yang, H. J. Kim, H. Jung, D. H. Chun and H. T. Lee, *Fuel*, 2010, **89**, 237–243.
60 C. J. Weststrate, A. C. Kazalkaya, E. T. R. Rossen, M. W. G. M. Verhoeven, I. M. Ciobîcă, A. M. Saib and J. W. Niemantsverdriet, *J. Phys. Chem. C*, 2012, **116**, 11575–11583.
61 N. E. Tsakoumis, M. Rønning, Ø. Borg, E. Rytter and A. Holmen, *Catal. Today*, 2010, **154**, 162–182.
62 I. M. Ciobîcă, R. A. van Santen, P. J. van Berge and J. van de Loosdrecht, *Surf. Sci.*, 2008, **602**, 17–27.
63 J. C. W. Swart, I. M. Ciobîcă, R. A. Van Santen and E. Van Steen, *J. Phys. Chem. C*, 2008, **112**, 12899–12904.
64 N. E. Tsakoumis, M. Rønning, Ø. Borg, E. Rytter and A. Holmen, *Catal. Today*, 2010, **154**, 162–182.
65 M. A. Petersen, J. A. Van Den Berg, I. M. Ciobîcă and P. Van Helden, *ACS Catal.*, 2017, **7**, 1984–1992.
66 J. X. Liu, H. Y. Su, D. P. Sun, B. Y. Zhang and W. X. Li, *J. Am. Chem. Soc.*, 2013, **135**, 16284–16287.
67 Y. Tison, K. Nielsen, D. J. Mowbray, L. Bech, C. Holse, F. Calle-Vallejo, K. Andersen, J. J. Mortensen, K. W. Jacobsen and J. H. Nielsen, *J. Phys. Chem. C*, 2012, **116**, 14350–14359.
68 S. Lyu, L. Wang, J. Zhang, C. Liu, J. Sun, B. Peng, Y. Wang, K. G. Rappé, Y. Zhang, J. Li and L. Nie, *ACS Catal.*, 2018, **8**, 7787–7798.
69 W. Chen, B. Zijlstra, I. A. W. Filot, R. Pestman and E. J. M. Hensen, *ChemCatChem*, 2018, **10**, 136–140.
70 B. Zijlstra, R. J. P. Broos, W. Chen, I. A. W. Filot and E. J. M. Hensen, *Catal. Today*, 2020, **342**, 131–141.
71 B. Zijlstra, R. J. P. Broos, W. Chen, G. L. Bezemer, I. A. W. Filot and E. J. M. Hensen, *ACS Catal.*, 2020, **10**, 9376–9400.
72 B. Böller, K. M. Durner and J. Wintterlin, *Nat. Catal.*, 2019, **2**, 1027–1034.
73 P. Van Helden, J. A. Van Den Berg, M. A. Petersen, W. Janse Van Rensburg, I. M. Ciobîcă and J. Van De Loosdrecht, *Faraday Discuss.*, 2017, **197**, 117–151.
74 N. Yang, A. J. Medford, X. Liu, F. Studt, T. Bligaard, S. F. Bent and J. K. Nørskov, *J. Am. Chem. Soc.*, 2016, **138**, 3705–3714.
75 M. Ehrensperger and J. Wintterlin, *J. Catal.*, 2014, **319**, 274–282.
76 M. Rønning, N. E. Tsakoumis, A. Voronov, R. E. Johnsen, P. Norby, W. Van Beek, Ø. Borg, E. Rytter and A. Holmen, *Catal. Today*, 2010, **155**, 289–295.
77 N. E. Tsakoumis, A. Voronov, M. Ronning, W. Van Beek, O. Borg, E. Rytter and A. Holmen, *J. Catal.*, 2012, **291**, 138–148.
78 A. Rochet, V. Moizan, C. Pichon, F. Diehl, A. Berliet and V. Briois, *Catalysis Today*, 2011, **171**, 186–191.
79 D. J. Moodley, A. M. Saib, J. Van De Loosdrecht, C. A. Welker-Nieuwoudt, B. H. Sigwebela and J. W. Niemantsverdriet, *Catal. Today*, 2011, **171**, 192–200.

80 A. M. Saib, A. Borgna, J. van de Loosdrecht, P. J. van Berge and J. W. Niemantsverdriet, *Appl. Catal., A*, 2006, **312**, 12–19.
81 E. Van Steen, M. Claeys, M. E. Dry, J. Van De Loosdrecht, E. L. Viljoen and J. L. Visagie, *J. Phys. Chem. B*, 2005, **109**, 3575–3577.
82 N. L. Visser, O. Daoura, P. N. Plessow, L. C. J. Smulders, J. W. de Rijk, J. A. Stewart, B. D. Vandegehuchte, F. Studt, J. E. S. van der Hoeven and P. E. de Jongh, *ChemCatChem*, 2022, **14**, e202200665.
83 R. Ouyang, J. X. Liu and W. X. Li, *J. Am. Chem. Soc.*, 2013, **135**, 1760–1771.
84 W. Janse Van Rensburg, P. Van Helden, D. J. Moodley, M. Claeys, M. A. Petersen and E. Van Steen, *J. Phys. Chem. C*, 2017, **121**, 16739–16753.
85 M. Claeys, M. E. Dry, E. Van Steen, P. J. Van Berge, S. Booyens, R. Crous, P. Van Helden, J. Labuschagne, D. J. Moodley and A. M. Saib, *ACS Catal.*, 2015, **5**, 841–852.
86 D. Moodley, M. Claeys, E. van Steen, P. van Helden, D. Kistamurthy, K. J. Weststrate, H. Niemantsverdriet, A. Saib, W. Erasmus and J. van de Loosdrecht, *Catal. Today*, 2020, **342**, 59–70.
87 D. Kistamurthy, A. M. Saib, D. J. Moodley, J. W. Niemantsverdriet and C. J. Weststrate, *J. Catal.*, 2015, **328**, 123–129.